UC Merced
UC Merced Previously Published Works

Title
Single Molecule Profiling of Molecular Recognition at a Model Electrochemical Biosensor

Permalink

Journal

ISSN

Authors
Gu, Qufei
Nanney, Warren
Cao, Huan H
et al.

Publication Date
2018-10-31

DOI

Peer reviewed

Single Molecule Profiling of Molecular Recognition at a Model Electrochemical Biosensor

Qufei Gu[†], Warren Nanney[‡], Huan H. Cao[‡], Haiyang Wang[†], and Tao Ye*[,‡]

[†]School of Engineering and [‡]School of Natural Sciences, University of California, Merced, 5200 N Lake Rd., Merced, California, 95343, United States

ABSTRACT: The spatial arrangement of target and probe molecules on the biosensor is a key aspect of the biointerface structure that ultimately determines the properties of interfacial molecular recognition and the performance of the biosensor. However, the spatial patterns of single molecules on practical biosensors have been unknown, making it difficult to rationally engineer biosensors. Here we have used high resolution atomic force microscopy to map closely spaced individual probes as well as discrete hybridization events on a functioning electrochemical DNA sensor surface. We also applied spatial statistical methods to characterize the spatial patterns at the single molecule level. We observed the emergence of heterogeneous spatiotemporal patterns of surface hybridization of hairpin probes. The clustering of target capture suggests that hybridization may be enhanced by proximity of probes and targets that are about 10 nm away. The unexpected enhancement was rationalized by the complex interplay between the nanoscale spatial organization of probe molecules, the conformational changes of the probe molecules, and target binding. Such molecular level knowledge may allow one to tailor the spatial patterns of the biosensor surfaces to improve the sensitivity and reproducibility.

INTRODUCTION

Biosensors typically consist of recognition elements immobilized on the surfaces of the transducer materials. For example, the electrochemical DNA biosensors,[1-2] which hold significant potential in point-of-care diagnostics due to their abilities in highly selective, label-free, and miniaturized detection of a range of biomarkers in complex biofluids,[3] immobilize nucleic acid capture probes onto the electrode surfaces. Molecular recognition is influenced by the interactions between the probe and the biointerface, which consists of neighboring probe molecules and captured biomarkers (target molecules), the passivating layer, the solid substrate (planar[3] or nanostructured surfaces[4-5]), and the solution.[6-7] An outstanding challenge is that the influences of the biointerface are complex and difficult to predict, hampering the effort to form biosensors with predictable performance. Extensive studies have explored the effects of probe design,[8] probe surface density,[9-12] surface chemistry,[13-14] and surface morphology.[15] However, one aspect that has remained poorly understood is how the nanoscale lateral organization of probe and captured target molecules influences molecular recognition. The spatial organization is a key aspect of the biointerface structure that ultimately determines the complex interactions and the properties of interfacial molecular recognition. The heterogeneous local density of probe molecules was thought to have difficult-to-predict influences on the accessibility of target molecules to the probe molecules (crowding interactions).[9, 16-17] Numerous studies provided indirect evidence that the impacts of the poorly controlled, often heterogeneous spatial organization of probe molecules[18] may be profound: they may not only limit detection sensitivity[4, 16] but also be the root cause of the large device-to-device signal variabilities[6, 19-22] of many of these surface-based sensors devices. Immobilization procedures that enhance probe dispersion[18] were found to improve reproducibility in target binding.[20, 22-23] Moreover, the attachment of probes to nanoscale DNA tetrahedra

increased the target binding rate by orders of magnitude.[16, 24-25] It was proposed that the footprint of the tetrahedral structures helps maintain uniform inter-probe separations and facilitate target binding.

However, a definitive correlation between nanoscale spatial patterns and interfacial molecular recognition had not been possible as existing techniques cannot resolve single molecules on biosensors.[26-27] On a practical biosensor surface with a probe density in the range of 10^{10}-10^{13}/cm^2,[7, 28] many of the molecules are separated by less than 10 nm, which is beyond the resolving power of existing techniques. Although few techniques, such as fluorescence microscopy,[27, 29-30] atomic force microscopy[31] and surface plasmon resonance[32] have detected single recognition events, single molecule imaging was only achieved on surfaces with extremely dilute coverages. Hence, almost all existing studies relied on the overall surface densities as the key parameter to describe how surface immobilization impacts molecular recognition.[9, 26, 33] While such studies have revealed general trends suggesting that surface crowding by probe molecules[9, 16-17] and captured targets[34] inhibits target recognition, these ensemble averaging observables are not adequate descriptors of the crowding interactions, especially in light of growing evidence that a realistic biosensor may be highly heterogeneous in probe density.[6, 18] In addition, the difficulty is compounded by the complex influences of other surface heterogeneities such as surface morphology,[35] surface chemistry, and molecular conformations.[6-7]

Previously, using surfaces that can switch interactions with DNA on demand,[18, 36-37] we have enabled atomic force microscopy (AFM) to spatially resolve single DNA molecules that are tethered to self-assembled monolayers (SAMs) on gold.[38] However, the previous work did not shed light on the complex relationship between the surface structure of the DNA probes and the hybridization, because the surface hybridization kinetics was characterized using the overall hybridization yield, which is an ensemble-averaging observable that
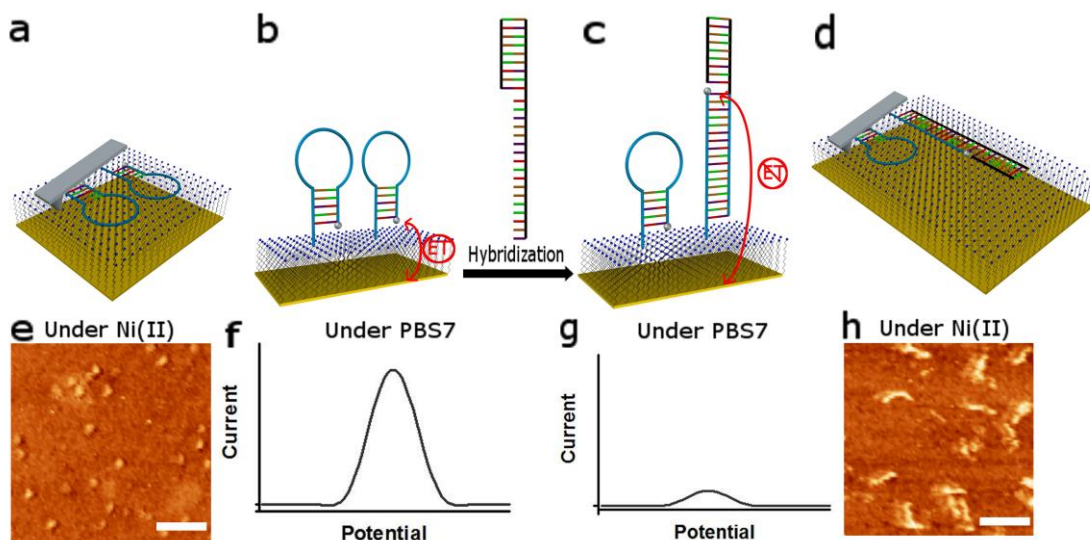
Figure 1. Schematic of a dynamically switchable E-DNA sensor surface. (a) A stem-loop DNA probe is covalently tethered at one end to a single-crystal Au electrode passivated with a MUDA monolayer and modified with a MB tag (Silver) at the other end. The probe is pinned down to the surface after adding Ni^{2+} and thus can be imaged by AFM. (b) After imaging, the surface is rinsed with an STAE buffer and a DPV measurement is carried out under a PBS7 buffer. (c) Upon the addition of a complementary target DNA into the PBS7 buffer, the same DPV measurement is repeated. (d) The hybridized surface is imaged following the same procedure as given in step (a) above. AFM images and DPV signals of the sensor surface (e,f) before and (h,g) after the hybridization with the targets. The scale bar is 25 nm.

obscures important details of an intrinsically heterogeneous system. In addition, how the surface structure impacts the electrochemical signals was unknown as the imaging was not carried out on functioning electrochemical sensors.

To address the above challenges, we have investigated for the first time how the spatial patterns of single probe molecules impact the molecular recognition of a functioning biosensor. We constructed model surfaces that serve as electrochemical DNA sensors and simultaneously utilized AFM to spatially resolve surface hybridization even when the inter-probe separation is less than 10 nm, allowing us to probe the regime where crowding interactions are important. The surfaces, which consist of electroactive DNA probes tethered to highly ordered SAMs, make it possible to modulate interaction with DNA,[36] and provide an ideal platform for investigating how spatial organization of single molecules alters molecular recognition as these surfaces minimize the impact of uncontrolled morphological and compositional heterogeneities. Moreover, by applying spatial statistical tools including Ripley's K function,[39-41] nearest-neighbor distances, local crowding indices to characterize spatial heterogeneities in target binding,[18] our study revealed unexpected spatiotemporal patterns of surface hybridization. The hybridization yields of probe molecules were observed to vary substantially with the nearest neighbor-distance. Hybridization of DNA targets with hairpin probes preferentially occurs where the probes are clustered, suggesting that the interactions between molecules separated by ~10 nm may facilitate target binding. The cooperative effect, in contrast with the prevailing view that increasing molecular crowding inhibits target capturing,[9, 17, 33] suggests new mechanisms through which the biosensor surface can influence target binding.

Our study provided the first direct evidence that the nanoscale spatial distribution of probe molecules exerts a major influence on surface hybridization. As the sensitivity of a biosensor is directly linked to interfacial molecular recognition, our findings have ramifications in biosensor design. The dramatic effect of the nearest-neighbor distance on hybridization suggests a new pathway to

improve the sensitivity: we may tailor the spatial patterns to favor inter-probe separations that maximize target binding efficiency. It should also be noted that the nanoscale spatial organization likely has important but undetermined influences on almost all surface-based biosensors.[4, 42-43] In addition to surface hybridization, our approach of combining spatially resolved measurement on model surfaces with single molecule spatial statistical analysis may be applied to other types of molecular recognition, such as aptamer sensors that detect proteins.[25, 44-45] How complex intermolecular interactions at the surface/interface influence the pathways of target recognition remain largely unknown. Therefore, probing and analyzing these biointerfaces at the molecular scale will lead to valuable insight that can help improve the performance of these biosensors.

RESULTS AND DISSCUSSION

To investigate target recognition by electrochemical DNA sensors at the single molecule level, we assembled a 11-mercaptoundecanoic acid (MUDA) SAM on single-crystal Au(111) disk electrodes, then 23-base stem-loop probes (P1) possessing a terminal thiol on the 5' end and a methylene blue (MB) redox reporter[46] on the 3' end were tethered to the SAM (insertion method, see Methods for details), which generates a relatively uniform probe distribution[18] as opposed to the conventional backfilling method (Figure S1).[12] Similar negatively charged SAMs have been used for electrochemical DNA sensors in previous studies.[13, 47] The probes can be strongly immobilized on the MUDA SAM in the presence of Ni^{2+} (Figure 1a), appearing as circular protrusions of ~8 nm diameter (Figure 1e).[36] Importantly, these immobilized probes can return to their upright state by replacing the Ni^{2+} buffer with a saline Tris-acetate-EDTA (STAE) buffer to enable both differential pulse voltammetry (DPV) measurement and target hybridization (Figure 1b, c). The sensor surface produces a well-resolved DPV peak, whereas after the addition of target DNAs, the peak signal drops (Figure 1f, g). We employed a target containing a 19-base single-stranded sticky-end, a 2-base spacer, and 19-bp double-stranded
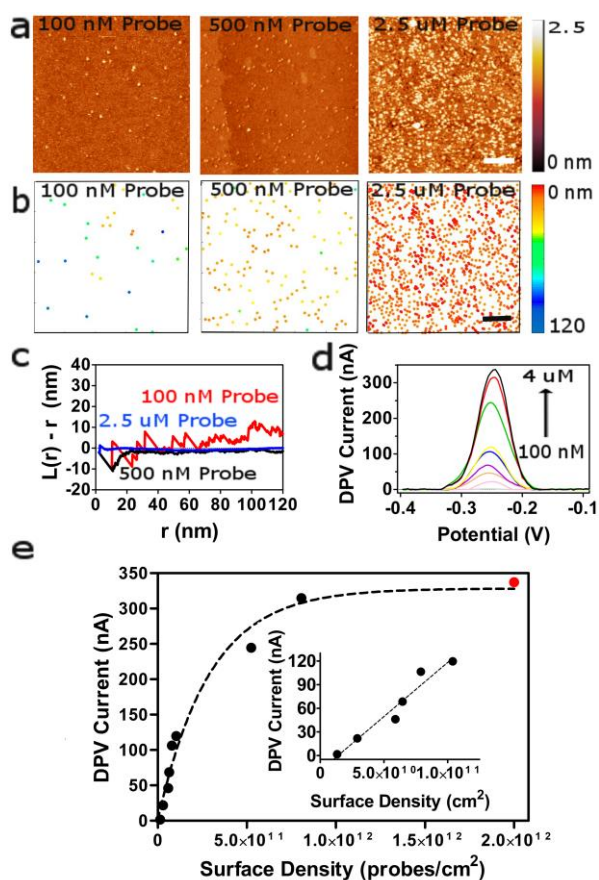
Figure 2. Correlating probe density and DPV of the E-DNA sensor surface. (a) Representative AFM images of the sensor surface fabricated using DNA probe concentrations at 100 nM, 500 nM and 2.5 μM. The insertion time is fixed at 30 min. The scale bar is 100 nm. (b) The nearest-neighbor distance (N.N.D.) analysis of probes in panel (a). The color bar indicates the range of N.N.D. from 0 nm (red) to 120 nm (blue). (c) The Ripley's K-function analysis of the distribution of probes. (d) The corresponding DPV voltammograms (from bottom to top). (e) The relation between probe surface density and peak current. Inset, the current peak of E-DNA sensor is linearly related to the probe surface density at low probe densities ($< 10^{11}$ probes/cm^2). Red dot represents the estimated probe density.

segment (T1). The double-stranded tail was designed to facilitate AFM identification of the target-probe duplexes. In addition, the target can to some extent mimic the larger footprints of nucleic acid targets used in clinical settings, which are often 150-300 nt in length, *i.e.*, much longer than the DNA capture probes (20-50 nt in length).[7, 34] The radius of gyration of the P1-T1 duplex is about 18 nm, which is similar to that of a target probe duplex that has a 20-bp double-stranded segment and 150-nt single-stranded segment.[7, 48] The AFM images of the surface before and after hybridization showed distinct features that correspond to unhybridized hairpin probes (Figure 1e) and P1-T1 duplexes (~20 nm long worm-like protrusions, Figure 1h).

Based on the above platform, we first explored how the probe densities can be controlled. The MUDA SAM was exposed to solutions containing different concentrations of thiolated DNA probes, ranging from 100 nM to 4 μM, as depicted in Figure 2a (as well as in Figure S2a), the probe surface density steadily rises when the concentration of thiolated DNA probes is increased. When the concentration is 4 μM, the resulting immobilized individual probe molecules are difficult to resolve due to significant overlap between

the molecular features. Hence only a lower limit, 2×10^{12} probes/cm^2 could be estimated. As listed in Table 1 (supporting information), these values cover most of the range of probe surface densities of biosensors and microarrays used in practice, except for the high end, 10^{12}-10^{13}/cm^2.[7, 10] While single molecule imaging can directly quantify the probe densities, we also utilized the unique ability to characterize the spatial patterns of single molecules, which are inaccessible with existing averaging techniques.[33, 49-50] First, we calculated the Ripley's K function, which can characterize the tendency for the probe molecules to cluster or disperse at different spatial scales.

$$K(r) = \lambda^{-1} E = \lambda^{-1} \sum_i \sum_{j \neq i} w(l_i, l_j)^{-1} \frac{I(d_{i,j} < r)}{N} \quad (1)$$

where λ is the number density of the molecules, E is the number of molecules within a radius of r from the molecule of interest, $w(l_i, l_j)$ the weight function for edge correction, I is the indicator function.[39] For a surface with a completely random spatial pattern,

$$[\frac{K(r)}{\pi}]^{\frac{1}{2}} - r = L(r) - r = 0 \quad (2)$$

Statistically significant clustering or dispersion can be identified by comparing measured L(r) - r against Monte Carlo simulated L(r) - r curves (Figure S2). All L(r) - r curves, except for those with very low probe densities (1.33×10^{10} and 2.91×10^{10} /cm^2, where fluctuation in L(r) - r is significant due to sparsity), lie close to the expected value of 0 for all distances up to 150 nm, implying an overall spatially random distribution of probes (Figure 2c and S2b). An exception is
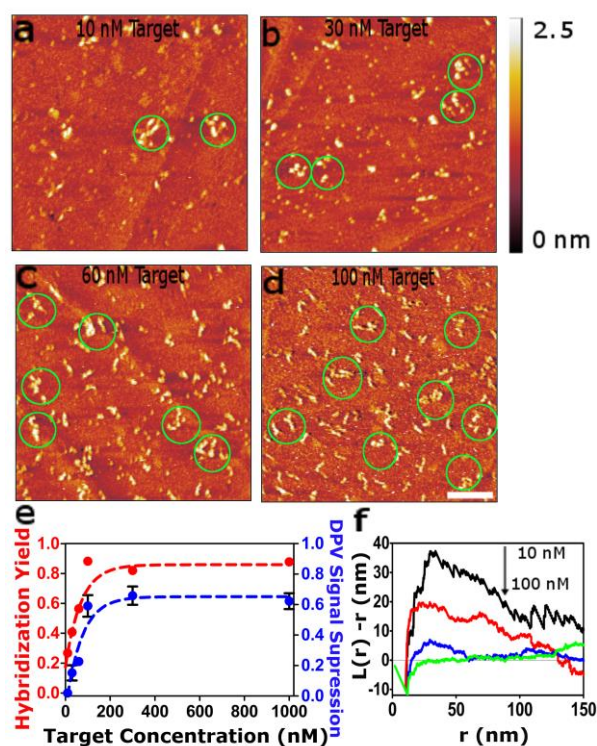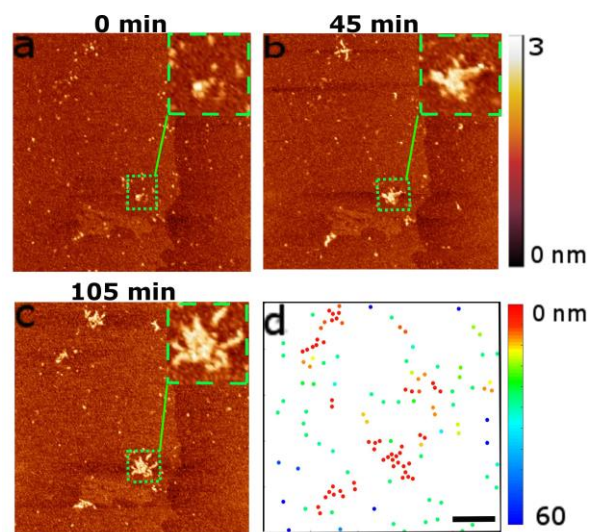

Figure 3. Spatial patterns of surface hybridization. (a-d) Representative AFM images of the sensor surface in the presence of complementary T1 target DNAs at 10 nM, 30 nM, 60 nM and 100 nM. The green dotted circles are used to outline the clusters. The hybridization time is fixed at 30 min. The scale bar is 100 nm. (e) The relation between hybridization yield (red curve) and DPV signal suppression (blue curve) at different target concentrations. (f) The Ripley's K-function analysis of the distribution of hybridized probes. The L(r) - r curve shows a decrease of clustering with increasing target concentration (from top to bottom).

that for surfaces with medium probe densities (5.90×10^{10}–1.04×10^{11} /cm^2), the L(r) - r values dip below the 2.5% quantile of Mont Carlo simulated L(r) - r values at 10 nm (black curve of Figure 2c and red curves of Figure S2b). The statistically significant deviation reveals the tendency for the probe molecules to be dispersed at this scale. The dispersion may be caused by the repulsive interactions between the molecules during probe immobilization, especially under our low ionic strength conditions (50 mM NaAc). The absence of dispersion at higher probe densities (blue curve in Figure 2c) suggests that the repulsive interactions are overcome by a larger driving force to pack the surface with probe molecules. While the Ripley's K function characterizes dispersion/clustering for the entire surface, a spatial property that likely has a direct effect on target recognition is the nearest neighbor distance (N.N.D.). Using the spatial coordinates, we displayed the N.N.D. of each of the probe molecules in the heat map in Figure 2b. The range of N.N.D. values is very broad. However, as shown in Ripley's K function (Figure 2c), the broad distribution of N.N.D. is a consequence of random distribution instead of clustering of molecules. Notably, the histograms of N.N.D. (Figure S2c), shows that up to 94.4% of the values are below the commonly used average probe separation, $<N.N.D.>_{Lat} = (A/n)^{1/2}$,[10, 33, 51-52] which is calculated assuming that the molecules are arranged in a square lattice, using A, the total surface area, and n, the number of molecules. The discrepancy clearly shows the reliability of the average inter-probe separation as the descriptor of crowding interactions is limited.

We then explored the correlation between the electrochemical signal and the overall probe density. The peak current increased as the DNA probe concentration increased from 100 nM to 4 μM (Figure 2d). More importantly, Figure 2e shows that the peak current scaled linearly with the probe density from 1.3×10^{10} to 1.0×10^{11} probes/cm^2, then began to level off at 5.2×10^{11} probes/cm^2. The saturation in peak current and the decline in peak current/probe density ratio suggests that the interactions between the probe molecules may induce the unfolding of the hairpin probe,[53-55] separating the redox reporter from the electrode surface and reducing the rate of electron transfer. Alternatively, as the inter-probe separations are reduced, the repulsive interactions between

Figure 4. Tracking evolution of heterogeneous spatial patterns of DNA surface hybridization. Representative AFM images of the sensor surface after exposed to 10 nM target DNA for (a) 0 min, (b) 45 min and (c) 105 min. The scale bar is 100 nm. Insets are zoom in images of green-squared areas. (d) The nearest-neighbor distance (N.N.D.) analysis of unhybridized probes in panel (a). The color bar indicates the range of N.N.D. from 10 nm (red) to 60 nm (blue).

probe molecules led to subtle orientation/conformational changes[17, 34] that increased the separation between the redox label and the electrode surface. It should be noted that while the imaging resolution achieved (a few nm) is insufficient for distinguishing between the folded and unfolded states, the results above nevertheless provide direct evidence that molecular crowding impacts the electrochemical signals.

We next examined the correlation between the hybridization yield and electrochemical signal suppression. Specifically, we measured the signal suppression of a surface with a probe density of 5.9×10^{10}/cm^2, when the target concentration was varied between 10 nM to 1 μM (300 nM and 1 μM in Figure S3) at a fixed hybridization time of 30 min. AFM images of the sensor surface were acquired as
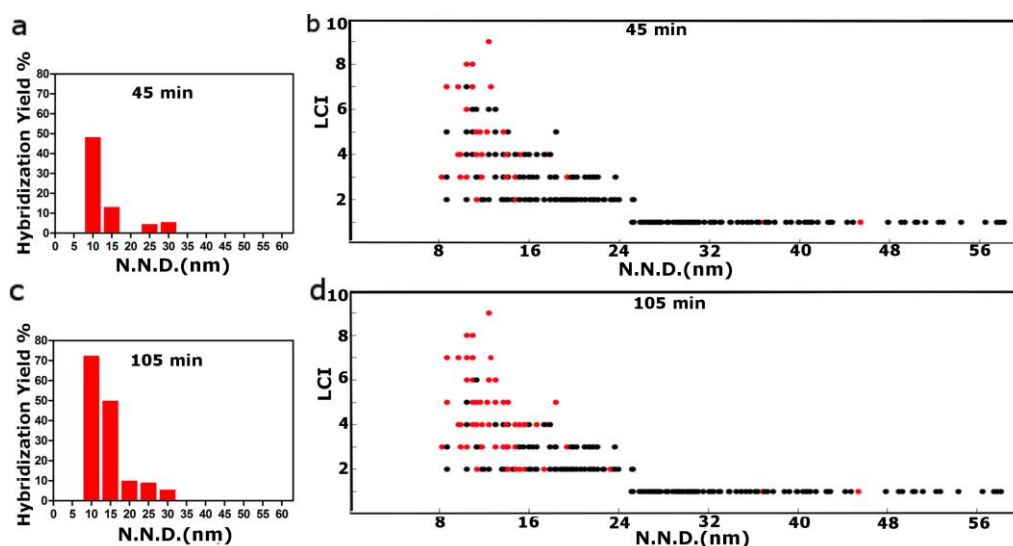
**Figure 5.** Spatial statistical analysis of probe distributions. (a), (c) The histograms of the hybridization yield at 45 min and 105 min as a function of N.N.D.. (b), (d) Plots of LCI *vs.* N.N.D. at 45 min and 105 min for each DNA probe. Probes with high LCI and low N.N.D. are more likely to capture targets. The red dots represent hybridized probes, while the black dots represent unhybridized probes.

well (Figure 3a-d) to directly quantify the overall hybridization yield. Figure 3e shows that the fraction of hybridized probes, *i.e.,* hybridization yield, increases with the increasing target concentration and reaches a plateau of 88% at 100 nM (red curve). The trend tracks the curve of the DPV signal suppression (blue curve). The gap between the hybridization yield curve and signal suppression curve is consistent with the observation that some of the probe/target duplexes have sufficient conformational freedom to tilt toward the surface for facile electron transfer, leading to incomplete signal suppression.[10] Moreover, while from electrochemical measurement alone, it is unclear whether the incomplete signal suppression is caused by the finite electron transfer rate or incomplete hybridization,[13] single molecule AFM analysis provides definitive evidence that a small fraction (~10%) of the probe molecules are inactive as no further enhancement in hybridization yield was observed even at higher target concentrations of 300 nM and 1 μM (Figure 3e and S3). A less than unity hybridization yield was also observed for hybridization in a homogeneous solution.[56] The origin is not yet clear. As the yield of each of the solid phase coupling reaction steps is below 100%, commercial synthetic oligonucleotides typically contain 10-15% impurities that are missing one or more nucleotides.[57] Therefore, one possibility is that these truncated oligonucleotides may be responsible for incomplete hybridization. In addition to concentration dependence, the hybridization yield was measured at different time intervals at a fixed target concentration of 100 nM. The hybridization yield increased over time and saturated after 30 minutes (Figure S4a). The same trend was found in the corresponding time evolution of DPV suppression (Figure S4b).

In addition to calibration-free, quantitative measurement of the overall hybridization yield, high resolution AFM imaging affords the unique opportunity to examine the spatial patterns of hybridization. Interestingly, we found that the probe-target duplexes tend to form clusters and the number of clusters grows with increasing target concentrations (Figure 3a-d, highlighted by green circles). To develop a more quantitative description, we analyzed the spatial distribution of these duplexes using the Ripley's K function. The positive values in Figure 3f show that the duplexes are clustered. The values approach zero with increasing target concentrations,

presumably due to the merging of clusters (L(r) – r curves for 300 nM and 1 μM targets are shown in Figure S3c).[58]

The emergence of a heterogeneous spatial pattern of hybridization from a mostly random spatial distribution of probe molecules is rather surprising as crowding is thought to inhibit target binding. The spatial pattern suggests target capture is instead a cooperative process. To gain more mechanistic insights, we imaged the same areas of the sensor surface (5.9×10^{10}/cm^2) to track the evolution of the spatial patterns (Figure 4a-c). This experiment can provide direct information concerning how probe spatial organization affects the cluster distribution and the pathway of cluster formation. The areas in green squares enlarged in the insets of Figure 4a-c show that the cluster started to emerge at 45 min and evolved into a complete cluster at 105 min at 10 nM target concentration. The nearest-neighbor distances (N.N.D.) map in Figure 4d showed that the captured target molecules predominantly appeared in the regions where the N.N.D. are less than or equal to 15 nm (red or orange dots). The histograms in Figure 5a and 5c further confirm that the hybridization of the probes is highly sensitive to N.N.D.. The fraction of hybridized probes with N.N.D. of 10 nm is close to 50%, while only 5% of the probes with N.N.D. of 25 nm are hybridized. These results provide evidence that under certain conditions, the crowding interactions between the molecules may enhance instead of inhibiting target binding. Moreover, we also used the local crowding index LCI(r), a parameter we introduced in a previous work,[18] to explore if molecules that are located beyond nearest-neighbors also impact hybridization. LCI(r) counts the number of neighboring probes surrounding a particular probe, within an interaction radius r (20 nm which is about twice the length of probe P1 is used here). A measure of the local probe density at a specific spatial scale, LCI(r) enables us to assess the degree of local crowding experienced by individual probes, which can then be correlated to their hybridization efficiency. Compared to N.N.D., which serves an indicator of the "two-body" interactions between the probe of interest and its nearest neighbor, LCI(r) allows us to examine our system from "many-body" perspective of neighboring probes. The LCI (20nm) versus N.N.D. plots at 45 min and 105 min (Figure 5b, d) show that the probability of hybridized probe molecules (red dots) increases at the top. For probe molecules with the same N.N.D., those with higher LCIs are more likely hybridize.
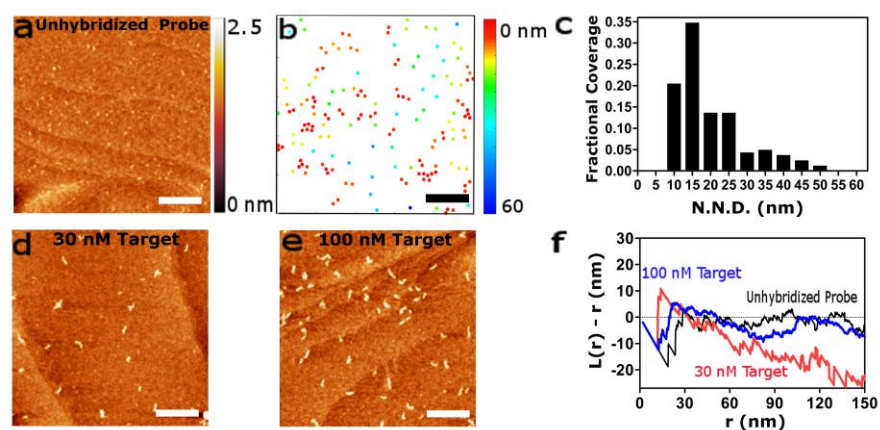
Figure 6. Control experiment using linear probes. Representative AFM images of the linear probe surface in the absence (a) and presence of complementary target DNAs at 30 nM (d) and 100 nM (e). The hybridization time is fixed at 15 min. The scale bar is 100 nm. (b) The nearest-neighbor distance (N.N.D.) analysis of unhybridized probes in panel (a). The color bar indicates the range of N.N.D from 10 nm (red) to 60 nm (blue). Histograms of unhybridized probes in panel (a) as a function of N.N.D.. (f) The Ripley's K-function analysis of the distribution of hybridized probes. The L(r) - r curves show uniform distributions of unhybridized probes (black) and hybridized probes at 100 nM (blue), and a relatively dispersed distribution of hybridized probes at 30 nM (red).

Overall, Figure 5 suggests that the presence of neighboring molecules (~15 nm) may accelerate the hybridization rate of the hairpin probes by an order of magnitude or more. Moreover, molecules that are located beyond the nearest-neighbors can also impose crowding interactions that accelerate hybridization.

To confirm that the local crowding of probe molecules is responsible for enhanced hybridization, we need to exclude the possibility that clustered probe molecules may coincide with disordered SAM domains that may accelerate hybridization through nonspecific adsorption on a more hydrophobic surface.[27] A previous study suggested that hydrophobic surfaces increase the residence time of the DNA targets and enhance the rate of hybridization.[59] No features of target molecules could be observed with AFM when a MUDA SAM without capture probes was exposed to the same target solution, indicating that only targets binding to the captured probes can remain on the surface and non-specific adsorption on SAM domains is weak (Figure S5). Moreover, we replaced the hairpin probe P1 with a linear probe P2 (Figure 6). Interestingly, although the probe surface density and spatial pattern of immobilized P2 molecules (Figure 6b, c) are similar to those of P1 (Figure 4d and S6), the spatial pattern of P2-T1 duplexes is substantially different (Figure 6d, e). The clustering function reveals a random spatial pattern of P2-T1 duplexes (Figure 6f). The absence of target clustering on surfaces with P2 shows that nonspecific adsorption on local SAM domains is not responsible for clustering of target-probe duplexes. The absence also rules out the possibility that the aggregation of target molecules in the solution is responsible for the clustering of captured targets with the hairpin probe P1. Another piece of supporting evidence is that clustering of captured targets is observed at target concentrations as low as 10 nM in a monovalent cation Na^+ buffer. Dynamic light scattering (DLS) measurements of the target solutions used for hybridization showed no aggregation (Figure S7). Consistent with previous studies, aggregation of DNAs in a monovalent buffer solution only occurs at higher concentrations (μM or more).[60-62] Therefore, we conclude that the clustering is caused by a combination of the secondary structure of the probe and a higher local probe density. Furthermore, we performed a hybridization experiment that used P1 to capture T2, which is a shorter, 19-base single-stranded counterpart of T1. Ripley's K function analysis also revealed a random spatial pattern of the P1-T2 duplexes under the same experimental conditions, including probe surface density, target concentration and hybridization time (Figure S8).

The observed spatial heterogeneity can be attributed to two distinct characteristics of the surface immobilized probes. First, the crowding interactions are more important for surface immobilized probe molecules than for probes in a solution. The average distance between DNA probes on a biosensor surface ranges from a few nanometers to tens of nanometers.[7, 28] In contrast, the average distance in a homogeneous solution is typically 100 nm or more, as the typical probe concentration is less than micromolar. Second, while the hybridized and unhybridized probes undergo free Brownian motion in solution hybridization, the surface tethered probes maintain their positions relative to the surface. Therefore, the interactions with neighboring molecules in a dilute solution are short-lived. In contrast, the spatial heterogeneity of surface immobilized probes is persistent (Figure 4a-c) and hence can affect hybridization kinetics as well as affinity substantially.

Our study provides the first single molecule level evidence that the spatial proximity of probe molecules has a major impact on target recognition. However, our findings are a departure from the prevailing assumption that surface crowding hinders target recognition and optimal hybridization kinetics is achieved at the lowest densities.[9-10, 12, 17, 26, 33] Two factors could be responsible for the discrepancy. First, as existing studies measured the overall target binding kinetics of surfaces that have highly heterogeneous inter-probe seperations,[18, 21, 63] it has not been possible to quantify the influences of specific inter-probe separations. Our single molecule resolution of hybridization represents an ideal way to address this question. In addition, many existing studies focus on high surface density regimes, $10^{12}/cm^2$ or greater,[9, 26, 33] where the accessibility to probe molecules may indeed be the limiting factor. Our study focuses on a less crowded regime ($\sim 10^{11}/cm^2$), where accessibility is less an issue and enhancement mechanisms may manifest themselves. The use of less perturbing imaging modes, such as noncontact AFM,[64] may allow AFM to study the single molecule spatial patterns at higher probe densities, when the probes are separated by less than a few nanometers, where limited accessibility to the probe molecules may begin to inhibit target binding.

The counter-intuitive cooperative effect may be rationalized by examining the microscopic mechanisms of DNA hybridization. The hybridization of a DNA hairpin probe is thought to proceed via a nucleation step that forms a stable contact between the loop and the target molecule, followed by the melting of the stem, and propagation of the base paired region to form a full probe-target duplex (zippering).[65] While the rate limiting step for hybridization of unstructured probes is the formation of stable target-probe contacts, that for hybridization of hairpin probes may be stem melting.[50, 65] When the probe molecules are separated by 10-15 nm, there is sufficient space for a target to form contacts with a probe. Based on the data either directly from this work or the literature,[66] we propose three mechanisms including (i) probe crowding, (ii) target crowding and (iii) crowding-induced surface trapping that may facilitate target recognition at these inter-probe distances. First, these probe molecules may impose a repulsive potential that destabilizes the hairpin structure of neighboring probe molecules and accelerates target binding.[10] Supporting evidence of this mechanism includes Figure 5 as well as the absence of clustering of target-probe duplexes using linear probes, P2 (Figure 6d-f). Moreover, the sublinear relationship between the electrochemical signal and the probe density when the probe density exceeds $1 \times 10^{11}/cm^2$ (Figure 2e) also suggests that probe crowding interaction favors the unfolded state. Unfolding of densely packed DNA hairpin probes was also observed in previous studies.[53, 55] While the probe density studied, $5.9 \times 10^{10}/cm^2$, appears too low to cause a significant fraction of them to unfold, our spatial statistical analysis shows that 20% of the probe molecules have N.N.D. of 10 nm or less (Figure S6) due to the random nature of spatial distribution. It should be noted that zippering does not need to be preceded by complete unfolding.[66] Even a modest destabilization of the hairpin may reduce the activation barrier of concomitant stem melting and formation of target-probe duplex and accelerate the kinetics. The second mechanism is the destabilization of the stem by binding of target molecules to nearby hairpins. A probe-target duplex increases electrostatic repulsion within a hemisphere, due to its ability to rotate around its anchor; the localized increase of electrostatic repulsion may also favor unfolding of neighboring hairpin probes and accelerate binding in close proximity. This target crowding is supported by the more facile hybridization of T1 compared to that of the shorter target, T2 (Figure S8). It should be noted that as many nucleic acid targets for molecular diagnostics are notably longer than the capture probes,[7, 34] this target crowding-induced cooperative effect is likely relevant. The third enhancement mechanism is that probe molecules in proximity can

6

trap the target molecules and increase their residence time. The formation of a full duplex is typically preceded by many unproductive contacts between the target and the hairpin loop.[66] A target molecule that is transiently bound may have a greater opportunity to hop onto a neighboring probe molecule and get captured. So far, no single mechanism could explain all the findings. While there is direct evidence supporting the first two mechanisms, probe crowding and target crowding, we cannot exclude the possibility that the third mechanism also contributes to the enhancement. Future studies that systematically explore the effects of target size, probe design and probe density can elucidate the relative contributions of the proposed mechanisms.

CONCLUSION

Spatially resolved measurement of molecular recognition of an E-DNA sensor revealed novel complex, heterogeneous behaviors that are difficult to capture using ensemble averaging techniques. Even when the probe density is relatively uniform, the wide distribution of inter-probe distances arising from random probe immobilization may lead to heterogeneous target binding. Therefore, the probe density alone may not be a reliable predictor of interfacial molecular recognition, given the observed major impact of inter-probe distances on target binding. These findings set the stage for future studies that can explore how these probe spatial patterns help determine the sensitivity and device to device variabilities of existing electrochemical biosensors.[6, 19-21] Moreover, it would be intriguing to explore the extent to which the spatial patterns impact the selectivity. Ultimately, the mechanistic insights from spatially resolved measurements and single molecule spatial statistical analysis may help establish a predictive relationship between molecular scale spatial patterns and the performance of the biosensor, paving the way toward the rational engineering of biosensor devices.

MATERIALS AND METHODS

Preparation of E-DNA sensors. Unless otherwise stated, all chemicals were obtained from Fisher Scientific Co. (Pittsburg, PA, USA). Insertion Method: An Au (111) single crystal disk (MaTeck GmbH, Juelich, Germany) substrate was used for both electrochemical measurement and AFM imaging. The Au single crystal disk was cleaned following a standard protocol [36-37] and then immersed into 1 mM MUDA (Sigma-Aldrich Co., St. Louis, MO, USA) solution in 9:1 ethanol (VWR, Radnor, PA, USA):acetic acid for 1 h. The disulfide DNA probes (P1 or P2) were reduced in 2mM TCEP (Tris-(2-carboxyethyl)-phosphate, Sigma-Aldrich Co., St. Louis, MO, USA) at room temperature for 20 min and then purified using a QIAquick Nucleotide Removal Kit (QIAGEN, Germantown, MD, USA) and stored at -20 °C. After 1 h, the Au substrate was thoroughly rinsed with 9:1 ethanol:acetic acid and water, blown dried with filtered air, and incubated with a buffer containing the thiolated DNA probes, 50 mM NaAc, and 2 mM TCEP for 30 minutes. Following the insertion step, the substrate was rinsed 3 times with a TAE (40 mM Tris-acetate and 1 mM EDTA, pH 8.3) buffer to remove nonspecific probe adsorption. Backfilling Method: The cleaned Au single crystal disk was immersed into a buffer containing the 20 nM thiolated DNA probes, 50 mM NaAc, and 2 mM TCEP for 1 h. After DNA probe assembly, the Au disk substrate was backfilled with 1 mM MUDA solution in 9:1 ethanol:acetic acid for 3h. Following the backfilling step, the substrate was thoroughly rinsed with in 9:1 ethanol:acetic acid and TAE buffer.

E-DNA sensor hybridization and probe/target duplex denaturation. The hybridization was carried out by incubating the sensor surface with a buffer containing DNA targets (T1 or T2), 1x PBS7 (10 mM Phosphate, 1M NaCl, pH 7) at room temperature in the dark. After a predetermined hybridization time, the sensor surface was then rinsed 3 times with an STAE buffer (1x TAE, 200 mM NaCl) to remove nonspecific adsorbed targets. To perform the kinetic study of the hybridization, the sensor surface was regenerated by immersion in an alkaline buffer (1x AB = 10 mM NaOH, 330 μM EDTA, pH 12) for 5 minutes after each target incubation, followed by thorough rinsing with STAE to remove the denatured targets. The denatured sensor surface is shown in Figure S9.

Electrochemical measurement. All DPV measurements was performed relative to an Ag/AgCl (3M KCl) reference electrode at room temperature using an Epsilon electrochemical analyzer (BASI, West Lafayette, IN, USA). The potential range was from -0.4 to -0.1 V and the pulse amplitude was 50 mV. An Au single crystal disk was used as a working electrode, together with a platinum counter electrode. In all experiment, the PBS7 was used as the electrolyte.

AFM imaging. All AFM images were obtained using Agilent/Keysight 5500 AFM (Keysight Technologies, Santa Rosa, CA, USA) and Ntegra Vita AFM (NT-MDT Co., Moscow, Russia) equipped with SNL-10 cantilevers (spring constants of 0.2-0.4 N/m, Bruker, Bellerica, MA, USA) under a Ni^{2+} buffer (5 mM $NiAc_2$, 0.1x TAE). Intermittent contact mode AFM imaging with a resonant frequency of approximately 16 kHz was performed. After imaging, the sensor surface was thoroughly rinsed with the STAE buffer to remove Ni^{2+}.

Probe density and hybridization yield quantification. To measure the probe densities, AFM imaging was carried out in at least four different areas of the Au substrate. An average probe density (molecules/area) in the absence of targets was determined by counting the number of corresponding features (8 nm diameter circular protrusions) in images using Gwyddion (http://gwyddion.net/) and WSxM[67] image analysis software. The number of hybridized probes after hybridization (~20 nm long worm-like protrusions) was determined in the same manner as the above. The hybridization yield was then defined as the number of hybridized probes divided by the total number of probes after hybridization.

Spatial statistical analysis of probe distribution. Gwyddion image analysis software was used to extract the XY-coordinates of DNA probes from AFM images. A mask was generated for all features that are above the minimal pixel area and height threshold. Minor manual editing was carried out to separate the partially overlapping features, especially for surfaces at higher probe densities. The coordinates of the centroids were then used to calculate the Ripley's $K(r)$ function as well as $[K(r)/\pi]^{1/2}$ - r = L(r) - r.[39] The observed $L(r)$ - r can be compared with the corresponding data under complete spatial randomness (CSR) computed by Monte Carlo simulation. 999 simulations were performed to reduce the sampling uncertainty and calculate the quantiles of $L(r)$ - r for each value of r, in which 0.025 and 0.975 quantiles were directly compared with $L(r)$ - r. The same coordinates were also used for N.N.D. and LCI analyses, where the former determines the distance between a probe and its closest neighboring probe, while the latter counts the number of surrounding probes with respect to a specific probe.

ASSCOIATED CONTENT

Supporting Information.

This material is available free of charge via the Internet on the ACS Publications website at

Materials and methods, summary of probe densities, images of the surface prepared using backfilling method, additional data and analysis of different probe densities and target concentrations, dynamic study of target hybridization, images of the SAM surface after exposure to the targets, N.N.D. distribution histogram for unhybridized probes, DLS measurement of target aggregation in solution, control experiment using small targets, and images of denatured surface (PDF)

AUTHOR INFORMATION

Corresponding Author

tao.ye@ucmerced.edu

Notes

The authors declare no competing financial interests.

ACKNOWLEDGMENT

REFERENCES

1. Drummond, T. G.; Hill, M. G.; Barton, J. K., Electrochemical DNA Sensors. *Nat. Biotechnol.* **2003,** *21* (10), 1192-1199.

2. Smith, S. J.; Nemr, C. R.; Kelley, S. O., Chemistry-Driven Approaches for Ultrasensitive Nucleic Acid Detection. *J. Am. Chem. Soc.* **2017,** *139* (3), 1020-1028.

3. Arroyo-Curras, N.; Somerson, J.; Vieira, P. A.; Ploense, K. L.; Kippin, T. E.; Plaxco, K. W., Real-Time Measurement of Small Molecules Directly in Awake, Ambulatory Animals. *Proc. Natl. Acad. Sci. U.S.A.* **2017,** *114* (4), 645-650.

4. Kelley, S. O.; Mirkin, C. A.; Walt, D. R.; Ismagilov, R. F.; Toner, M.; Sargent, E. H., Advancing the Speed, Sensitivity and Accuracy of Biomolecular Detection Using Multi-Length-Scale Engineering. *Nat. Nanotechnol.* **2014,** *9* (12), 969-980.

5. Liu, B.; Wu, P.; Huang, Z.; Ma, L.; Liu, J., Bromide as a Robust Backfiller on Gold for Precise Control of DNA Conformation and High Stability of Spherical Nucleic Acids. *J. Am. Chem. Soc.* **2018,** *140* (13), 4499-4502.

6. Bizzotto, D.; Burgess, I. J.; Doneux, T.; Sagara, T.; Yu, H. Z., Beyond Simple Cartoons: Challenges in Characterizing Electrochemical Biosensor Interfaces. *ACS Sensors* **2018,** *3* (1), 5-12.

7. Rao, A. N.; Grainger, D. W., Biophysical Properties of Nucleic Acids at Surfaces Relevant to Microarray Performance. *Biomater. Sci.* **2014,** *2* (4), 436-471.

8. Liu, Y. T.; Irving, D.; Qiao, W. Q.; Ge, D. B.; Levicky, R., Kinetic Mechanisms in Morpholino-DNA Surface Hybridization. *J. Am. Chem. Soc.* **2011,** *133* (30), 11588-11596.

9. Peterson, A. W.; Heaton, R. J.; Georgiadis, R. M., The Effect of Surface Probe Density on DNA Hybridization. *Nucleic Acids Res.* **2001,** *29* (24), 5163-5168.

10. Ricci, F.; Lai, R. Y.; Heeger, A. J.; Plaxco, K. W.; Sumner, J. J., Effect of Molecular Crowding on the Response of an Electrochemical DNA Sensor. *Langmuir* **2007,** *23* (12), 6827-6834.

11. Giljohann, D. A.; Seferos, D. S.; Patel, P. C.; Millstone, J. E.; Rosi, N. L.; Mirkin, C. A., Oligonucleotide Loading Determines Cellular Uptake of DNA-Modified Gold Nanoparticles. *Nano Lett.* **2007,** *7* (12), 3818-3821.

12. Herne, T. M.; Tarlov, M. J., Characterization of DNA Probes Immobilized on Gold Surfaces. *J. Am. Chem. Soc.* **1997,** *119* (38), 8916-8920.

13. Ricci, F.; Zari, N.; Caprio, F.; Recine, S.; Amine, A.; Moscone, D.; Palleschi, G.; Plaxco, K. W., Surface Chemistry Effects on the Performance of an Electrochemical DNA Sensor. *Bioelectrochemistry* **2009,** *76* (0), 208-213.

14. Kuralay, F.; Campuzano, S.; Wang, J., Greatly Extended Storage Stability of Electrochemical DNA Biosensors Using Ternary Thiolated Self-Assembled Monolayers. *Talanta* **2012,** *99*, 155-160.

15. Soleymani, L.; Fang, Z. C.; Sargent, E. H.; Kelley, S. O., Programming the Detection Limits of Biosensors through Controlled Nanostructuring. *Nat. Nanotechnol.* **2009,** *4* (12), 844-848.

16. Pei, H.; Lu, N.; Wen, Y. L.; Song, S. P.; Liu, Y.; Yan, H.; Fan, C. H., A DNA Nanostructure-Based Biomolecular Probe Carrier Platform for Electrochemical Biosensing. *Adv. Mater.* **2010,** *22* (42), 4754-4758.

17. Morrin, G. M.; Schwartz, D. K., Three Regimes of Polymer Surface Dynamics under Crowded Conditions. *Macromolecules* **2018,** *51* (3), 1207-1214.

18. Josephs, E. A.; Ye, T., Nanoscale Spatial Distribution of Thiolated DNA on Model Nucleic Acid Sensor Surfaces. *ACS Nano* **2013,** *7* (4), 3653-3660.

19. Li, H.; Dauphin-Ducharme, P.; Ortega, G.; Plaxco, K. W., Calibration-Free Electrochemical Biosensors Supporting Accurate Molecular Measurements Directly in Undiluted Whole Blood. *J. Am. Chem. Soc.* **2017,** *139* (32), 11207-11213.

20. Yang, L.; Zhang, C. H.; Jiang, H.; Li, G. J.; Wang, J. H.; Wang, E. K., Insertion Approach: Bolstering the Reproducibility of Electrochemical Signal Amplification Via DNA Superstructures. *Anal. Chem.* **2014,** *86* (10), 4657-4662.

21. Du, H.; Disney, M. D.; Miller, B. L.; Krauss, T. D., Hybridization-Based Unquenching of DNA Hairpins on Au Surfaces: Prototypical "Molecular Beacon" Biosensors. *J. Am. Chem. Soc.* **2003,** *125* (14), 4012-4013.

22. Cao, H. H.; Nakatsuka, N.; Serino, A. C.; Liao, W. S.; Cheunkar, S.; Yang, H. Y.; Weiss, P. S.; Andrews, A. M., Controlled DNA Patterning by Chemical Lift-Off Lithography: Matrix Matters. *ACS Nano* **2015,** *9* (11), 11439-11454.

23. Macazo, F. C.; Karpel, R. L.; White, R. J., Monitoring Cooperative Binding Using Electrochemical DNA-Based Sensors. *Langmuir* **2015,** *31* (2), 868-875.

24. Wen, Y. L.; Pei, H.; Wan, Y.; Su, Y.; Huang, Q.; Song, S. P.; Fan, C. H., DNA Nanostructure-Decorated Surfaces for Enhanced Aptamer-Target Binding and Electrochemical Cocaine Sensors. *Anal. Chem.* **2011,** *83* (19), 7418-7423.

25. Wang, S.; Zhang, L. Q.; Wan, S.; Cansiz, S.; Cui, C.; Liu, Y.; Cai, R.; Hong, C. Y.; Teng, I. T.; Shi, M. L.; Wu, Y.; Dong, Y. Y.; Tan, W. H., Aptasensor with Expanded Nucleotide Using DNA Nanotetrahedra for Electrochemical Detection of Cancerous Exosomes. *ACS Nano* **2017,** *11* (4), 3943-3949.

26. Mirmomtaz, E.; Castronovo, M.; Grunwald, C.; Bano, F.; Scaini, D.; Ensafi, A. A.; Scoles, G.; Casalis, L., Quantitative Study of the Effect of Coverage on the Hybridization Efficiency of Surface-Bound DNA Nanostructures. *Nano Lett.* **2008,** *8* (12), 4134-4139.

27. Monserud, J. H.; Schwartz, D. K., Mechanisms of Surface-Mediated DNA Hybridization. *ACS Nano* **2014,** *8* (5), 4488-4499.

28. Cutler, J. I.; Auyeung, E.; Mirkin, C. A., Spherical Nucleic Acids. *J. Am. Chem. Soc.* **2012,** *134* (3), 1376-1391.

29. Peterson, E. M.; Manhart, M. W.; Harris, J. M., Single-Molecule Fluorescence Imaging of Interfacial DNA Hybridization Kinetics at Selective Capture Surfaces. *Anal. Chem.* **2016,** *88* (2), 1345-1354.

30. Lu, X.; Nicovich, P. R.; Gaus, K.; Gooding, J. J., Towards Single Molecule Biosensors Using Super-Resolution Fluorescence Microscopy. *Biosensors & Bioelectronics* **2017,** *93*, 1-8.

31. Husale, S.; Persson, H. H. J.; Sahin, O., DNA Nanomechanics Allows Direct Digital Detection of Complementary DNA and Microrna Targets. *Nature* **2009,** *462* (7276), 1075-1078.

32. Zijlstra, P.; Paulo, P. M. R.; Orrit, M., Optical Detection of Single Non-Absorbing Molecules Using the Surface Plasmon Resonance of a Gold Nanorod. *Nat. Nanotechnol.* **2012,** *7* (6), 379-382.

33. Gong, P.; Levicky, R., DNA Surface Hybridization Regimes. *Proc. Natl. Acad. Sci. U.S.A.* **2008,** *105* (14), 5301-5306.

34. Halperin, A.; Buhot, A.; Zhulina, E. B., Brush Effects on DNA Chips: Thermodynamics, Kinetics, and Design Guidelines. *Biophys. J.* **2005,** *89* (2), 796-811.

35. Hao, X.; Josephs, E. A.; Gu, Q.; Ye, T., Molecular Conformations of DNA Targets Captured by Model Nanoarrays. *Nanoscale* **2017,** *9* (36), 13419-13424.

36. Abel, G. R., Jr.; Josephs, E. A.; Luong, N.; Ye, T., A Switchable Surface Enables Visualization of Single DNA Hybridization Events with Atomic Force Microscopy. *J. Am. Chem. Soc.* **2013,** *135* (17), 6399-6402.

37. Josephs, E. A.; Ye, T., A Single-Molecule View of Conformational Switching of DNA Tethered to a Gold Electrode. *J. Am. Chem. Soc.* **2012,** *134* (24), 10021-10030.

38. Gooding, J. J.; Ciampi, S., The Molecular Level Modification of Surfaces: From Self-Assembled Monolayers to Complex Molecular Assemblies. *Chem. Soc. Rev.* **2011,** *40* (5), 2704-2718.

39. Haase, P., Spatial Pattern-Analysis in Ecology Based on Ripley K-Function: Introduction and Methods of Edge Correction. *J. Veg. Sci.* **1995,** *6* (4), 575-582.

40. Kiskowski, M. A.; Hancock, J. F.; Kenworthy, A. K., On the Use of Ripley's K-Function and Its Derivatives to Analyze Domain Size. *Biophys. J.* **2009,** *97* (4), 1095-1103.

41. Goreaud, F.; Pelissier, R., On Explicit Formulas of Edge Effect Correction for Ripley's K-Function. *J. Veg. Sci.* **1999,** *10* (3), 433-438.

42. Luo, X. L.; Davis, J. J., Electrical Biosensors and the Label Free Detection of Protein Disease Biomarkers. *Chem. Soc. Rev.* **2013,** *42* (13), 5944-5962.

43. Sassolas, A.; Blum, L. J.; Leca-Bouvier, B. D., Immobilization Strategies to Develop Enzymatic Biosensors. *Biotechnol. Adv.* **2012,** *30* (3), 489-511.

44. Xiao, Y.; Lubin, A. A.; Heeger, A. J.; Plaxco, K. W., Label-Free Electronic Detection of Thrombin in Blood Serum by Using an Aptamer-Based Sensor. *Angew. Chem. Int. Edit.* **2005,** *44* (34), 5456-5459.

45. Xiao, Y.; Piorek, B. D.; Plaxco, K. W.; Heeger, A. J., A Reagentless Signal-on Architecture for Electronic, Aptamer-Based Sensors Via Target-Induced Strand Displacement. *J. Am. Chem. Soc.* **2005,** *127* (51), 17990-17991.

46. Vallee-Belisle, A.; Plaxco, K. W., Structure-Switching Biosensors: Inspired by Nature. *Curr. Opin. Struc. Biol.* **2010,** *20* (4), 518-526.

47. Martens, I.; Fisher, E. A.; Bizzotto, D., Direct Mapping of Heterogeneous Surface Coverage in DNA-Functionalized Gold Surfaces with Correlated Electron and Fluorescence Microscopy. *Langmuir* **2018,** *34* (7), 2425-2431.

48. Sim, A. Y. L.; Lipfert, J.; Herschlag, D.; Doniach, S., Salt Dependence of the Radius of Gyration and Flexibility of Single-Stranded DNA in Solution Probed by Small-Angle X-Ray Scattering. *Phys. Rev. E* **2012,** *86* (2), 021901.

49. Steel, A. B.; Herne, T. M.; Tarlov, M. J., Electrochemical Quantitation of DNA Immobilized on Gold. *Anal. Chem.* **1998,** *70* (22), 4670-4677.

50. Gao, Y.; Wolf, L. K.; Georgiadis, R. M., Secondary Structure Effects on DNA Hybridization Kinetics: A Solution Versus Surface Comparison. *Nucleic Acids Res.* **2006,** *34* (11), 3370-3377.

51. White, R. J.; Phares, N.; Lubin, A. A.; Xiao, Y.; Plaxco, K. W., Optimization of Electrochemical Aptamer-Based Sensors Via Optimization of Probe Packing Density and Surface Chemistry. *Langmuir* **2008,** *24* (18), 10513-10518.

52. Wong, I. Y.; Melosh, N. A., An Electrostatic Model for DNA Surface Hybridization. *Biophys. J.* **2010,** *98* (12), 2954-2963.

53. Cederquist, K. B.; Golightly, R. S.; Keating, C. D., Molecular Beacon-Metal Nanowire Interface: Effect of Probe Sequence and Surface Coverage on Sensor Performance. *Langmuir* **2008,** *24* (16), 9162-9171.

54. Watkins, H. M.; Simon, A. J.; Ricci, F.; Plaxco, K. W., Effects of Crowding on the Stability of a Surface-Tethered Biopolymer: An Experimental Study of Folding in a Highly Crowded Regime. *J. Am. Chem. Soc.* **2014,** *136* (25), 8923-8927.

55. Cederquist, K. B.; Keating, C. D., Hybridization Efficiency of Molecular Beacons Bound to Gold Nanowires: Effect of Surface Coverage and Target Length. *Langmuir* **2010,** *26* (23), 18273-18280.

56. Zhang, J. X.; Fang, J. Z.; Duan, W.; Wu, L. R.; Zhang, A. W.; Dalchau, N.; Yordanov, B.; Petersen, R.; Phillips, A.; Zhang, D. Y., Predicting DNA Hybridization Kinetics from Sequence. *Nat. Chem.* **2018,** *10* (1), 91-98.

57. https://www.idtdna.com/pages/home.

58. Kiskowski, M. A.; Hancock, J. F.; Kenworthy, A. K., On the Use of Ripley's K-Function and Its Derivatives to Analyze Domain Size. *Biophys. J.* **2009,** *97* (4), 1095-1103.

59. Chan, V.; Graves, D. J.; McKenzie, S. E., The Biophysics of DNA Hybridization with Immobilized Oligonucleotide Probes. *Biophys. J.* **1995,** *69* (6), 2243-2255.

60. Rill, R. L., Liquid-Crystalline Phases in Concentrated Aqueous-Solutions of Na+ DNA. *Proc. Natl. Acad. Sci. U.S.A.* **1986,** *83* (2), 342-346.

61. Strzelecka, T. E.; Rill, R. L., Solid-State P-31 NMR-Studies of DNA Liquid-Crystalline Phases. The Isotropic to Cholesteric Transition. *J. Am. Chem. Soc.* **1987,** *109* (15), 4513-4518.

62. Strzelecka, T. E.; Davidson, M. W.; Rill, R. L., Multiple Liquid-Crystal Phases of DNA at High-Concentrations. *Nature* **1988,** *331* (6155), 457-460.

63. Murphy, J. N.; Cheng, A. K. H.; Yu, H. Z.; Bizzotto, D., On the Nature of DNA Self-Assembled Monolayers on Au: Measuring Surface Heterogeneity with Electrochemical in Situ Fluorescence Microscopy. *J. Am. Chem. Soc.* **2009,** *131* (11), 4042-4050.

64. Inada, N.; Asakawa, H.; Matsumoto, Y.; Fukuma, T., Molecular-Scale Surface Structures of Oligo (Ethylene Glycol)-Terminated Self-Assembled Monolayers Investigated by Frequency Modulation Atomic Force Microscopy in Aqueous Solution. *Nanotechnology* **2014,** *25* (30), 305602.

65. Yin, Y. D.; Zhao, X. S., Kinetics and Dynamics of DNA Hybridization. *Acc. Chem. Res.* **2011,** *44* (11), 1172-1181.

66. Chen, C. L.; Wang, W. J.; Wang, Z.; Wei, F.; Zhao, X. S., Influence of Secondary Structure on Kinetics and Reaction Mechanism of DNA Hybridization. *Nucleic Acids Res.* **2007,** *35* (9), 2875-2884.

67. Horcas, I.; Fernandez, R.; Gomez-Rodriguez, J. M.; Colchero, J.; Gomez-Herrero, J.; Baro, A. M., Wsxm: A Software for Scanning Probe Microscopy and a Tool for Nanotechnology. *Rev. Sci. Instrum.* **2007,** *78* (1), 013705.

For Table of Contents Only